5-1-2013

Loss of equilibrative nucleoside transporter 1 in mice leads to progressive ectopic mineralization of spinal tissues resembling diffuse idiopathic skeletal hyperostosis in humans

Sumeeta Warraich
Schulich School of Medicine & Dentistry

Derek B.J. Bone
Schulich School of Medicine & Dentistry

Diana Quinonez
Schulich School of Medicine & Dentistry

Hisataka Ii
Schulich School of Medicine & Dentistry

Doo Sup Choi
Mayo Medical School

See next page for additional authors

ORIGINAL ARTICLE

JBMR

Loss of Equilibrative Nucleoside Transporter 1 in Mice Leads to Progressive Ectopic Mineralization of Spinal Tissues Resembling Diffuse Idiopathic Skeletal Hyperostosis in Humans

Sumeeta Warraich,[1]* Derek BJ Bone,[1]* Diana Quinonez,[1] Hisataka Ii,[1] Doo-Sup Choi,[2] David W Holdsworth,[3] Maria Drangova,[3] S Jeffrey Dixon,[1] Cheryle A Séguin,[1†] and James R Hammond[1†]

[1]Department of Physiology and Pharmacology, Schulich School of Medicine & Dentistry, The University of Western Ontario, London, ON, Canada

[2]Department of Molecular Pharmacology and Experimental Therapeutics, Mayo Clinic College of Medicine, Rochester, MN, USA

[3]Imaging Research Laboratories, Robarts Research Institute, The University of Western Ontario, London, ON, Canada

ABSTRACT

Diffuse idiopathic skeletal hyperostosis (DISH) is a noninflammatory spondyloarthropathy, characterized by ectopic calcification of spinal tissues. Symptoms include spine pain and stiffness, and in severe cases dysphagia and spinal cord compression. The etiology of DISH is unknown and there are no specific treatments. Recent studies have suggested a role for purine metabolism in the regulation of biomineralization. Equilibrative nucleoside transporter 1 (ENT1) transfers hydrophilic nucleosides, such as adenosine, across the plasma membrane. In mice lacking ENT1, we observed the development of calcified lesions resembling DISH. By 12 months of age, *ENT1*$^{-/-}$ mice exhibited signs of spine stiffness, hind limb dysfunction, and paralysis. Micro–computed tomography (μCT) revealed ectopic mineralization of paraspinal tissues in the cervical-thoracic region at 2 months of age, which extended to the lumbar and caudal regions with advancing age. Energy-dispersive X-ray microanalysis of lesions revealed a high content of calcium and phosphorus with a ratio similar to that of cortical bone. At 12 months of age, histological examination of *ENT1*$^{-/-}$ mice revealed large, irregular accumulations of eosinophilic material in paraspinal ligaments and entheses, intervertebral discs, and sternocostal articulations. There was no evidence of mineralization in appendicular joints or blood vessels, indicating specificity for the axial skeleton. Plasma adenosine levels were significantly greater in *ENT1*$^{-/-}$ mice than in wild-type, consistent with loss of ENT1—a primary adenosine uptake pathway. There was a significant reduction in the expression of *Enpp1*, *Ank*, and *Alpl* in intervertebral discs from *ENT1*$^{-/-}$ mice compared to wild-type mice. Elevated plasma levels of inorganic pyrophosphate in *ENT1*$^{-/-}$ mice indicated generalized disruption of pyrophosphate homeostasis. This is the first report of a role for ENT1 in regulating the calcification of soft tissues. Moreover, *ENT1*$^{-/-}$ mice may be a useful model for investigating pathogenesis and evaluating therapeutics for the prevention of mineralization in DISH and related disorders.

KEY WORDS: CALCIFICATION; MICRO–COMPUTED TOMOGRAPHY; ADENOSINE; INTERVERTEBRAL DISC; SPINAL HYPEROSTOSIS

Introduction

Abnormal calcification of the extracellular matrix of soft connective tissues is associated with a number of pathologies including vascular disease, chronic kidney disease, and multiple skeletal disorders.[1–4] Ossification of paraspinal ligaments is often detected in middle-aged and elderly patients, presenting as one of two noninflammatory spondyloarthropathies: (1) diffuse idiopathic skeletal hyperostosis (DISH; formerly referred to as Forestier disease), which involves calcification of

Received in original form May 31, 2012; revised form October 23, 2012; accepted November 12, 2012. Accepted manuscript online November 26, 2012.
Address correspondence to: Cheryle A Séguin, PhD, Department of Physiology and Pharmacology, Schulich School of Medicine & Dentistry, The University of Western Ontario, London, Ontario, Canada N6A 5C1. E-mail: cheryle.seguin@schulich.uwo.ca

Current address: DBJB, Molecular Signaling Section, Laboratory of Bioorganic Chemistry, National Institute of Diabetes Digestive and Kidney Diseases, National Institutes of Health, Bethesda, MD, USA.

Current address: JRH, Department of Pharmacology, University of Alberta, Edmonton, AB, Canada.

*SW and DBJB contributed equally to this work.

†CAS and JRH contributed equally to this work.

Additional Supporting Information may be found in the online version of this article

Journal of Bone and Mineral Research, Vol. 28, No. 5, May 2013, pp 1135–1149

DOI: 10.1002/jbmr.1826

spinal ligaments and extra-axial structures including entheses[4]; and (2) ossification of the posterior longitudinal ligament (OPLL), which is common in the Japanese population.[5] Although often misdiagnosed, DISH and OPLL are distinct from degenerative disc disease, osteoarthritis, and ankylosing spondylitis.[6]

DISH is typically diagnosed using radiographs of the thoracic spine or chest, which demonstrate: (1) flowing calcifications along the anterolateral aspect of at least four contiguous vertebral bodies; (2) preservation of intervertebral disc height (in contrast to degenerative disc disease); and (3) absence of bony ankylosis of facet joints and absence of sacroiliac erosion, sclerosis, or fusion (in contrast to ankylosing spondylitis).[7] DISH often manifests as back pain associated with limited range of spinal motion, but can progress to the extent that lesions interfere with neighboring structures, including compression of the spinal cord and nerve roots.[8,9] Lesions in DISH can also cause dysphagia,[10] and DISH is associated with increased susceptibility to spinal fractures[11] and postsurgical heterotopic ossifications.[12] Correlative studies have associated obesity, hypertension, diabetes mellitus, hyperinsulinemia, dyslipidemia, elevated growth hormone levels, elevated insulin-like growth factor-1, and hyperuricemia with DISH.[13–15] It has been proposed that DISH lesions originate in fibrocartilaginous structures including entheses[16]; however, due to the lack of suitable animal models, the underlying pathogenesis remains obscure.

Several factors including genetic background have been postulated to be involved in the etiology of DISH; however, to date no single gene defect has been associated with the disease. In a subset of DISH patients of Asian descent, single-nucleotide polymorphisms in the *COL6A1* and *FGF2* genes have been shown to confer genetic susceptibility to DISH.[17,18] In contrast to DISH, OPLL has been studied extensively in the Japanese population, leading to identification of a number of associated genes, including *NPSS*,[19,20] *COL11A*,[21] *COL6A1*,[22] *BMP2*,[23] *TGFβ*,[24] and *FGFR1*.[18]

Recent advances point to a critical role for purine metabolism in the regulation of biomineralization in diseases associated with either insufficient or ectopic mineralization.[25–30] For example, mutations in the gene encoding ectonucleotide pyrophosphatase/phosphodiesterase 1 (ENPP1) have been associated with hypermineralization disorders.[25,26] Moreover, a recent study has linked ectopic arterial and joint calcifications with loss of ecto-5′-nucleotidase (5′NTD) function leading to decreased levels of extracellular adenosine.[27] To further explore the role of purine metabolism in the regulation of biomineralization, we examined the phenotype of the mouse lacking the gene encoding the nucleoside transporter ENT1. ENT1 (equilibrative nucleoside transporter 1 or solute carrier family 29 member 1, encoded by the *Slc29a1* locus) is the predominant nucleoside transporter expressed in mammalian cells.[31] This sodium-independent, facilitative diffusion carrier is responsible for the movement of hydrophilic nucleosides, such as adenosine, across biological membranes. Loss of ENT1 activity would be expected to modify extracellular adenosine levels, thus altering overall purine metabolism and signaling through adenosine receptors. The present study reports the novel skeletal phenotype of the $ENT1^{-/-}$ mouse that resembles DISH in humans.

Subjects and Methods

Animals

$ENT1^{-/-}$ mice were generated through targeted deletion of exons 2 to 4 of the gene encoding ENT1 by a cre-loxP targeting strategy.[32] $ENT1^{-/-}$ mice were backcrossed with outbred C57BL/6 mice. The mouse colony was maintained through the breeding of heterozygous animals ($ENT1^{+/-}$) to obtain wild-type ($ENT1^{+/+}$) and knockout ($ENT1^{-/-}$) littermates. Mice were housed in standard cages and maintained on a 12-hour light/dark cycle, with rodent chow and water available *ad libitum*. Genotyping was performed as described.[33] Given the increased reported prevalence of DISH in males (25% of men versus 15% of women over 50 years of age),[34] male mice were used for all experiments. Mice were euthanized at the following ages: 1 month (4–4.5 weeks), 2 months (8–11 weeks), 4 months (16–18 weeks), 6 months (26–30 weeks), and 12+ months (12–17 months). Experimental results were derived from groups of at least 3 wild-type and 3 $ENT1^{-/-}$ mice. All aspects of this study were conducted in accordance with the policies and guidelines set forth by the Canadian Council on Animal Care and were approved by the Animal Use Subcommittee of the University of Western Ontario, London, ON, Canada.

Micro–computed tomography imaging

Micro–computed tomography (μCT) scanning, reconstruction, and analysis were performed based on reported protocols[35] with the following modifications. Formalin-fixed or snap-frozen whole mice were imaged at Robarts Research Institute (London, ON, Canada) using a dedicated laboratory μCT scanner (eXplore speCZT; GE Healthcare, Waukesha, WI, USA). Data were acquired with an X-ray tube voltage of 90 kV and a current of 40 mA. In one continuous rotation, 900 views were obtained at an angular increment of 0.4 degrees and an exposure interval of 16 ms per view. The total scan time was 5 minutes per animal. A calibrating phantom, consisting of a vial of water, air, and a synthetic bone-mimicking epoxy (SB3; Gammex Inc. Middleton, WI, USA), was imaged together with the specimens. Images were acquired at isotropic voxel size of 100 μm and reconstructed into 3D images, using a modified cone-beam algorithm.[36] The reconstructed data were expressed in Hounsfield units by calibrating the gray-level values against those of water and air. Mineralized tissue density within the volume of interest was expressed as hydroxyapatite (HA) equivalent density (mg HA cm^{-3}), based on the calibration provided by the SB3 bone-mimicking material.

Images acquired for each animal were scored for severity of ectopic mineralization, based on the percentage of affected sites within the spine (sites defined as an intervertebral disc and/or associated paraspinal ligaments and entheses) in each anatomical region (cervical, thoracic, lumbar, and caudal). Values ranged from 0 to 4, with a score of 0 reflecting no detectable mineralized lesions, 1 indicating lesions involving 0% to 30% of sites within the anatomical region, 2 indicating lesions involving 30% to 60% of sites, 3 indicating lesions involving 60% to 90% of sites, and 4 indicating lesions involving 90% to 100% of sites.

Measurement of mineralized tissue density

Using data acquired by μCT, quantification of the density and volume of mineralized tissues was performed in a region of interest restricted to the spine (C_1 to sacrum), rib cage, and sternum. For this purpose, a 3D volume of interest was defined by an operator within each volume image, using manually drawn contours lofted to create a volume that included only the anatomy of interest (MicroView 2.2; GE Healthcare Biosciences). Three measurements were obtained within this volume of interest: the volume of hypermineralized tissue, the volume of tissue with density equivalent to that of normal cortical bone, and the maximum density. Hypermineralized tissue was defined as material that exceeded the maximum density of cortical bone in the spine of wild-type mice within a specified age group. In the present study, we defined threshold values of 610, 630, and 710 mg HA cm^{-3} for maximum spinal bone density in animals of ages 2, 4, and 6 (or greater) months, respectively. Previous studies have reported a similar increase in murine cortical bone density during the first 24 weeks of postnatal development.[37] Normal density tissue was defined as material that exceeded a minimum threshold (126 mg HA cm^{-3}), but fell below the maximum thresholds defined above. Volume measurements are reported in cubic millimeters (mm^3), representing the summation of all the volume elements that fell within the defined range of mineral density. Additionally, the maximum mineralized tissue density within the volume of interest was reported. Nonlinear least squares fits were obtained using GraphPad Prism; data for volume of hypermineralized lesions were fit with an exponential growth equation, and data for the volume of normal bone and maximum density values were fit with one-phase association equations.

Scanning electron microscopy and energy-dispersive X-ray spectroscopy

Scanning electron microscopy (SEM) imaging and energy-dispersive X-ray spectroscopy (EDX) microanalyses were performed based on previous reports[38] using a LEO 1540XB FIB/SEM instrument (Carl Zeiss, Oberkochen, Germany) and X-ray analysis system (Oxford Instruments, Oxford, UK) at the Western Nanofabrication Facility (The University of Western Ontario). Prior to SEM imaging, dried samples were coated with 5 nm of osmium using a plasma coater (OPC-80T; Filgen Inc., Nagoya, Japan). EDX spectra were collected from bone and mineralized lesions identified by electron backscatter imaging at 20 keV beam energy. Elemental analysis of the EDX spectra was performed using INCA software (Oxford Instruments), including background correction and fitting of all peaks.

Histology

Formalin-fixed tissue samples were decalcified with Shandon TBD-2 Decalcifier (Thermo Scientific, Nepean, ON Canada) at a ratio of 10:1 (fluid:tissue) for 5 days with gentle rocking. Following standard histological processing, decalcified samples were embedded in paraffin and 5 μm-thick serial sections were cut. Tissues were sectioned, mounted on glass slides and baked for 48 hours at 45°C. Slides were stained with hematoxylin and eosin (H&E) and images were acquired using a Leica DM1000 microscope.

For visualization of cell nuclei, sections described above were dewaxed in xylene and rehydrated by successive immersion in descending concentrations of ethanol. Mounting was performed with VECTASHIELD Mounting Medium with 4′,6-diamidino-2-phenylindole (DAPI) (Burlingame, CA) and images were captured using a Leica DMI6000B microscope.

Blood chemistry

High-performance liquid chromatography (HPLC) was used to analyze plasma for levels of adenosine and adenosine metabolites to determine the functional consequence of loss of ENT1. At 2 months of age, mice were anesthetized with pentobarbital. Blood was collected by cardiac puncture into a syringe containing NaCl (118 mM), KCl (5 mM), EDTA (13.2 mM), 5-iodotubercidin (10 μM) to inhibit adenosine kinase, *erythro*-9-(2-hydroxy-3-nonyl)adenine hydrochloride (EHNA, 100 μM) to inhibit adenosine deaminase, and dilazep (10 μM) to inhibit adenosine transport.[39] Plasma was isolated by sedimentation at 3,000*g* for 10 minutes at 4°C. Plasma was applied to a 10-kDa cutoff ultrafiltration column and sedimented at 14,000*g* for 15 minutes at 4°C. Filtered plasma was analyzed on an Onyx monolithic C18 column as described,[40] using a Hewlett Packard 1090 LC with UV detector. Adenosine was detected at 260 nm and adenosine metabolites at 250 nm.

To screen for systemic changes resulting from loss of ENT1, serum chemistry was performed using established panels of clinical chemistry parameters. At 2 months of age, mice were anesthetized with pentobarbital and blood was collected by cardiac puncture. Blood was allowed to coagulate at room temperature for 30 minutes. Samples were then sedimented at 3,000*g* for 10 minutes at 4°C and the serum supernatant was transferred to a fresh tube and frozen at –80°C. Chemical and biochemical analyses were performed by the Centre for Modeling Human Disease at the Toronto Centre for Phenogenomics (Toronto, Canada).

To assay plasma levels of inorganic pyrophosphate (PP_i), mice were anesthetized with pentobarbital and blood was collected by cardiac puncture. Samples were transferred to microfuge tubes containing heparin (5 USP units/mL of blood) and plasma was isolated by sedimentation at 3,000*g* for 10 minutes at 4°C. Plasma was applied to 10-kDa cutoff ultrafiltration spin columns and sedimented at 14,000*g* for 20 minutes at 4°C. A fluorimetric PP_i assay kit (ab112155; Abcam, Cambridge, MA, USA) was first validated using plasma samples from wild-type mice. Selected samples were supplemented with a saturating concentration of PP_i (30 μM) in the presence or absence of inorganic pyrophosphatase (0.0012 units/μL of sample; Sigma-Aldrich, St. Louis, MO, USA) (Supplemental Fig. S1). Plasma samples were isolated from 2-month-old wild-type and *ENT1*$^{-/-}$ mice ($n = 6$ mice for each genotype) and analyzed according to the manufacturer's protocol with an incubation time of 20 minutes. Fluorescence was measured at excitation and emission wavelengths of 316 and 456 nm, respectively, using a SpectraMax M5 microplate reader (Molecular Devices, Sunnyvale, CA, USA) with Softmax Pro v5 software. Values were interpolated using linear regression. Background levels of plasma autofluorescence were negligible.

Quantitative real-time RT-PCR

At 6 months of age, littermate-paired wild-type and *ENT1*$^{-/-}$ mice ($n = 8$ for each genotype) were dissected to isolate intervertebral discs (IVDs). IVDs were segregated according to anatomical location as cervical-thoracic, lumbar, or caudal, and placed directly in TRIzol Reagent (Invitrogen, Life Technologies, Burlington, ON, Canada). The IVDs were homogenized using a Polytron benchtop homogenizer and total RNA was extracted according to the manufacturer's protocol. cDNA synthesis was performed using Superscript II Reverse Transcriptase (Invitrogen, Life Technologies). Gene expression patterns were determined by real-time PCR using the Bio-Rad CFX384 system. Gene transcript levels were determined by absolute quantification assays, using a six-point calibration curve made from known starting quantities of cDNA (0.1 μg to 3.2×10^{-5} μg) synthesized from a mix of wild-type heart, brain, kidney, muscle, intervertebral disc, and calvarial RNA. Values are expressed relative to the calibration curve. PCR primer sequences are provided in Supplemental Table 1.

Results

Ectopic mineralization in *ENT1*$^{-/-}$ mice

Previous studies reported that *ENT1*$^{-/-}$ mice are phenotypically normal, with only a modest decrease (~10%) in body weight compared with that of wild-type littermates.[32] At young ages, open-field locomotor activity in *ENT1*$^{-/-}$ and wild-type mice does not differ. Moreover, there is no significant difference in spontaneous mortality rates up to 6 months of age. To date, there have been no reports of phenotypic changes in skeletal tissues related to mineralization[32,33,41,42]; however, all reported studies were conducted on mice less than 4 months of age.

In the present study, we noted that the spines of 6-month-old *ENT1*$^{-/-}$ mice were extremely rigid. At 8 months, *ENT1*$^{-/-}$ mice demonstrated decreased hindlimb mobility that progressed to hindlimb paralysis by 12 to 17 months of age. Postmortem analysis of a 17-month-old *ENT1*$^{-/-}$ mouse revealed hard, chalky, white lesions protruding ventrally from the thoracic spine (Fig. 1*A*). μCT images revealed large radio-opaque lesions at distinct foci in the cervical and upper thoracic regions of *ENT1*$^{-/-}$ mice, localized to paraspinal and intervertebral tissues, and protruding in some cases into the spinal canal (Fig. 1*B*). Histological examination identified large accumulations of amorphous material (Fig. 1*C*) localized to the intervertebral discs (upper panel) and paraspinal tissues associated with the spinous processes (lower panel). The presence of calcified lesions within the spinal canal, impinging on the spinal cord, was consistent with the decreased mobility and paralysis observed in *ENT1*$^{-/-}$ mice.

Time course of phenotype development

μCT imaging was employed to assess the development and extent of ectopic mineralization in *ENT1*$^{-/-}$ mice over time (Fig. 2*A*). Images were scored for severity, based on the percentage of affected sites within the spine (intervertebral discs, and associated paraspinal ligaments and entheses) in each anatomical region (Fig. 2*B*). Ectopic mineralization of spinal tissues was not evident in wild-type animals at any time point (Fig. 2*A*), or in *ENT1*$^{-/-}$ mice at 1 month of age (not shown).

Ectopic mineralization in *ENT1*$^{-/-}$ mice proceeded temporally in a consistent anatomical pattern. At 2 months of age, maximum intensity projection (MIP) images revealed radio-opaque material in the paraspinal tissues of the cervical spine and the rib entheses of the upper thoracic spine (Fig. 2, top panels). At this age, there was no detectable involvement of intervertebral discs.

With advancing age, accumulation of ectopic mineral progressed caudally, with involvement of the lumbar spine at 6 months (Fig. 2, middle panels). In addition to paraspinal tissues and rib entheses, lesions were observed within the intervertebral spaces at 6 months in both the thoracic and lumbar spine. At this time point, lesions involved 60% to 90% of the cervical spine and 30% to 60% of the thoracic spine. Interestingly, lesions did not progress caudally in a uniform manner. Following involvement of the cervical and upper thoracic spine, lesion formation initially bypassed the mid-region of the thoracic spine and then appeared specifically in thoracic vertebrae T_{11}–T_{12} (Fig. 2*A*, asterisk). At greater ages, lesions developed in the intervening mid-region of the thoracic spine.

By 12 months of age, ectopic mineralization was detected in >60% of the cervical, thoracic, and lumbar regions of the spine,

Table 1. Mineralized Tissue Density in *ENT1*$^{-/-}$ and Wild-Type Mice

Age (months)	*ENT1*$^{-/-}$ Volume (mm^3) Hypermineralized	*ENT1*$^{-/-}$ Volume (mm^3) Normal	*ENT1*$^{-/-}$ Max density (mg HA cm^{-3})	Wild-Type Volume (mm^3) Hypermineralized	Wild-Type Volume (mm^3) Normal	Wild-Type Max density (mg HA cm^{-3})
12+	$16.4 \pm 3.2^{**}$ ($n = 4$)	$527 \pm 48^{*}$	$1044 \pm 77^{**}$	0.5 ± 0.4 ($n = 3$)	356 ± 35	744 ± 10
6	3.5 ± 1.1 ($n = 3$)	381 ± 55	$921 \pm 38^{*}$	0.6 ± 0.5 ($n = 3$)	351 ± 92	746 ± 54
4	1.9 ± 1.5 ($n = 3$)	341 ± 16	763 ± 110	0.5 ± 0.6 ($n = 3$)	318 ± 79	639 ± 65
2	0.4 ± 0.5 ($n = 4$)	256 ± 52	652 ± 84	0.5 ± 0.5 ($n = 4$)	259 ± 32	651 ± 58

μCT-derived values for the volume of normal and hypermineralized tissue and the maximum density in *ENT1*$^{-/-}$ and wild-type mice. Data are means ± SD. Differences were evaluated by two-way analysis of variance (ANOVA) followed by a Bonferroni multiple comparison test.

ENT1 = equilibrative nucleoside transporter 1; HA = hydroxyapatite.

Significantly different from wild-type: $^{*}p < 0.05$, $^{**}p < 0.001$.

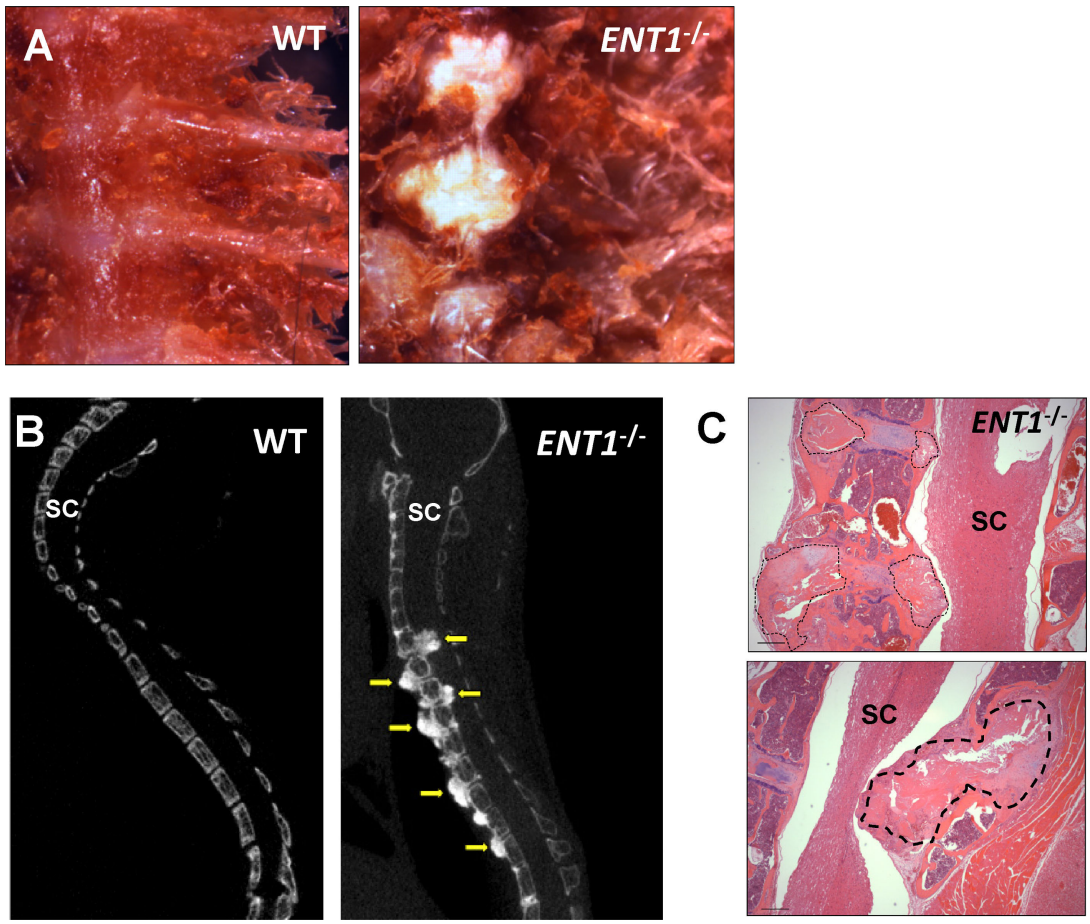

Fig. 1. Ectopic mineralization of spinal tissues in *ENT1*$^{-/-}$ mice. (*A*) Gross appearance of ventral aspect of the thoracic spine from 17-month-old wild-type (WT) and *ENT1*$^{-/-}$ mice. Mineralized lesions protrude from intervertebral spaces, associated with rib entheses. Lesions demonstrated hard, chalky consistency and were whitish in color. (*B*) Maximum intensity projection of μCT images showing the lateral aspect of the cervical and thoracic spine of 17-month-old WT and *ENT1*$^{-/-}$ mice. Ectopic radio-opaque material is evident in paraspinal and intervertebral regions of the spine (arrows) extending into the spinal canal (SC). (*C*) Histological sections of decalcified spinal tissues from 17-month-old *ENT1*$^{-/-}$ mouse (spinal column and spinal cord) stained with H&E. Mineralized lesion (outlined in black) can be seen protruding into the spinal canal and impinging on the spinal cord. Images in *B* and *C* are oriented with ventral to the left. Scale bars represent 200 μm.

as well as >30% of intervertebral discs of the caudal spine (Fig. 2, lower panel). In addition, there was notable decrease in kyphosis between 6 and 12 months of age in *ENT1*$^{-/-}$ mice compared to wild-type (Fig. 2*A*, lower panel). No evidence of ectopic mineralization was detected in the vasculature of *ENT1*$^{-/-}$ mice at any time point examined by μCT.

To examine the consequence of *ENT1* haploinsufficiency, 6-month-old heterozygous *ENT1*$^{+/-}$ mice were examined by μCT (Supplementary Fig. S2). In contrast to *ENT1*$^{-/-}$ mice, heterozygous animals did not demonstrate ectopic mineral formation in paraspinal tissues, rib entheses, or intervertebral discs. Moreover, the loss of kyphosis observed in knockout animals was not apparent; *ENT1* heterozygous animals were indistinguishable from wild-type controls.

Density and elemental composition of ectopic lesions

Mineralized tissue density of wild-type and *ENT1*$^{-/-}$ mice at different ages was quantified from μCT data. The region of interest for these analyses consisted of the cervical to lumbar spine, rib cage, and sternum. Hypermineralized tissue was detected in paraspinal and intervertebral tissues of the spine, as well as the sternocostal articulations (highlighted in red in Fig. 3*A*). Quantification revealed that the volume of hypermineralized tissue grew exponentially with age in the *ENT1*$^{-/-}$ mice, whereas there was little hypermineralized tissue detectable in wild-type mice at any age (Fig. 3*B*). We also quantified the volume of mineralized tissue with density equivalent to that of normal cortical bone (Fig. 3*C*). Whereas the wild-type animals appeared to reach a plateau of approximately 355 mm^3 by day 200 (reflecting bone growth), *ENT1*$^{-/-}$ mice reached a plateau of 552 mm^3 by day 400 (reflecting both bone growth and accumulation of ectopic mineral). Likewise, the maximum mineral density of the wild-type mice reached a plateau before an age of 200 days, whereas that of the *ENT1*$^{-/-}$ mice continued to increase past day 400 (Fig. 3*D*), reflecting hypermineralization of the ectopic lesions.

A summary and statistical analysis of these data is presented in Table 1. From 2 to 17 months of age, the volume of bone in wild-type mice increased from 259 to 356 mm^3 with only about

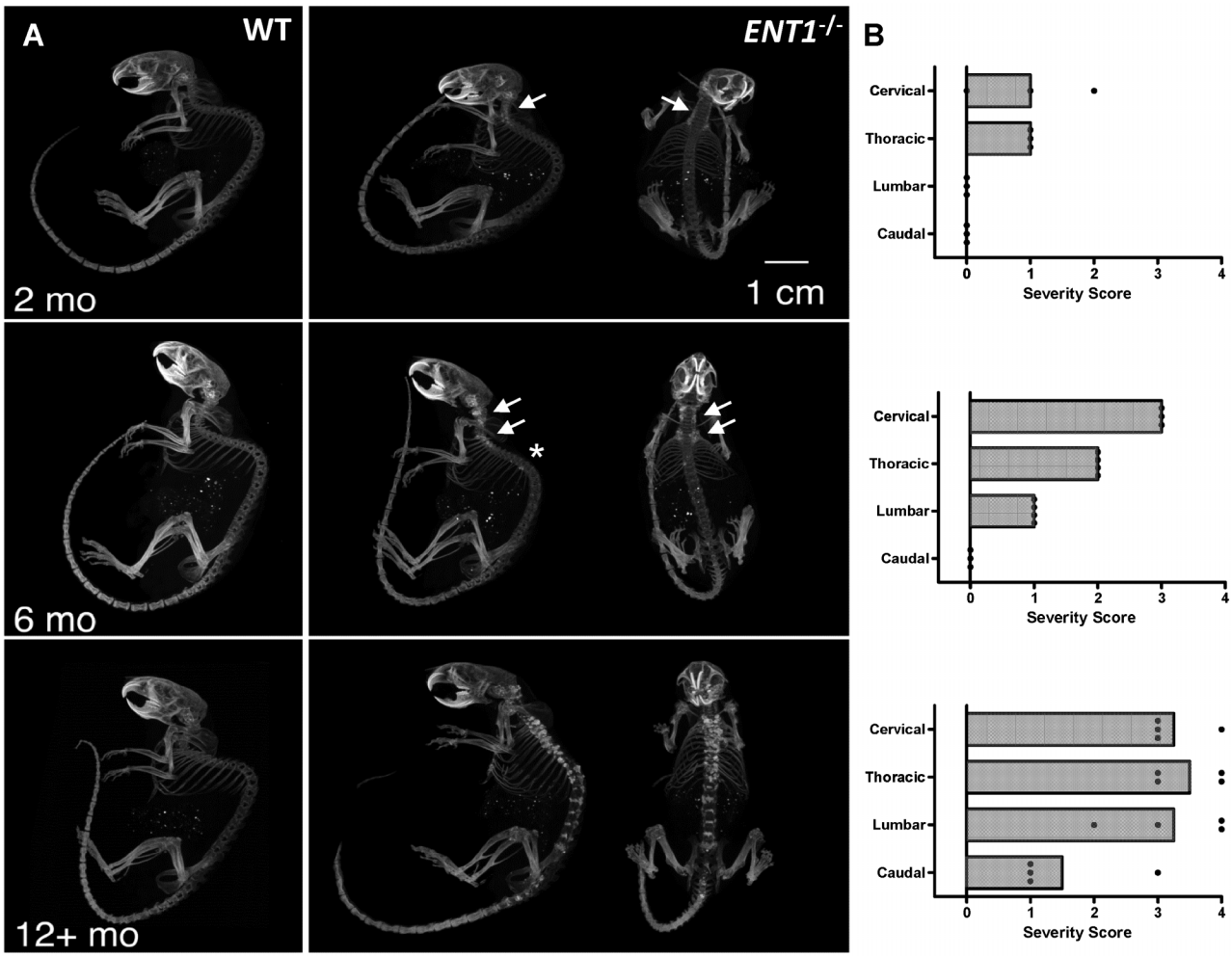

Fig. 2. Temporal progression of ectopic mineralization in *ENT1*$^{-/-}$ mice. (*A*) Lateral and anteroposterior maximum intensity projections of μCT images of wild-type (WT) and *ENT1*$^{-/-}$ mice at 2, 6, or 12+ months of age. Ectopic radio-opaque material was observed in paraspinal tissues of the cervical spine at 2 months of age (top panel, white arrows). By 6 months of age, lesions were detected in the cervical, thoracic, and lumbar spine in paraspinal ligaments, rib entheses, and intervertebral discs (white arrows, middle panel). At 6 months, lesions involved the upper thoracic spine, but appeared to bypass the mid-region of the thoracic spine to specifically affect sites in the vicinity of thoracic vertebrae T_{11}–T_{12} (indicated by white asterisk). By 12 months of age, lesions involved virtually the entire cervical, thoracic, and lumbar spine, and were detectable in the intervertebral discs of the caudal spine (lower panel). Note that the focal hyperintensities observed in the abdomen result from high-density material in the animal chow; these bright spots do not represent ectopic calcifications. (*B*) The percentage of sites affected by mineralization in each anatomical region of the spine was scored in *ENT1*$^{-/-}$ mice at 2, 6, or 12+ months of age. A severity score of 0 reflects no detectable mineralized lesions, 1 indicates lesions involving 0% to 30% of sites within the anatomical region, 2 indicates lesions involving 30% to 60% of sites, 3 indicates lesions involving 60% to 90% of sites, and a score of 4 indicates lesions involving 90% to 100% of sites. The symbols represent scores for individual mice and bars represent the mean.

0.5 mm^3 appearing hypermineralized (regardless of age) according to the thresholds used. The mineralized tissue volume of *ENT1*$^{-/-}$ mice was similar to that of wild-type controls up to 6 months of age. In contrast, 12- to 17-month-old *ENT1*$^{-/-}$ mice had a significantly greater volume of mineralized tissue than the equivalent age of wild-type mice (527 versus 356 mm^3). In addition, the *ENT1*$^{-/-}$ mice had a significantly greater volume of hypermineralized tissue than wild-type mice between 12 to 17 months old (16 versus 0.5 mm^3), and the maximum mineral density was significantly greater in *ENT1*$^{-/-}$ mice than wild-type controls at both 6 and 12 months of age. Note that whereas the maximum mineral density observed in *ENT1*$^{-/-}$ mice (1044 mg HA cm^{-3}) does not exceed the typical value for fully mineralized cortical bone (approximately 1050 mg HA cm^{-3}), it is significantly greater than the mineral density of cortical bone observed in the spine of wild-type littermates (744 mg HA cm^{-3}).

Samples from wild-type and *ENT1*$^{-/-}$ mice at 6 months of age were analyzed by EDX to determine the elemental content of both cortical bone and mineralized lesions. Mineralized lesions appeared by SEM as a disordered amorphous material (Supplemental Fig. S3*A*, *B*) and EDX revealed a high content of calcium and phosphorus (Supplemental Fig. S3*C*). The mean elemental content of bone and lesions is displayed as the percent atomic ratio in Table 2. The vertebral bone from *ENT1*$^{-/-}$ mice was not significantly different from that of wild-type mice in terms of elemental ratios. In contrast, ectopic mineralized lesions in *ENT1*$^{-/-}$ mice displayed higher levels of phosphorus and calcium relative to vertebral bone, consistent with the greater

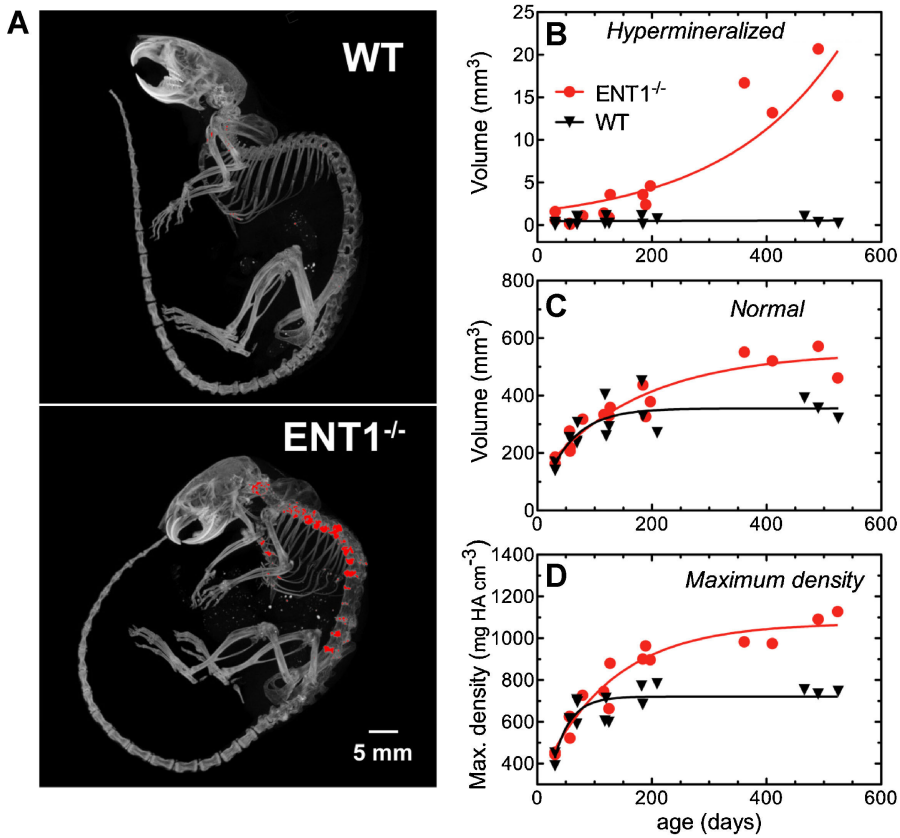

Fig. 3. Quantification of the volume and density of mineralized material in wild-type (WT) and *ENT1*$^{-/-}$ mice over time. (*A*) Lateral maximum intensity projections of the μCT images of a WT and an *ENT1*$^{-/-}$ mouse at 17 months of age. The region of interest for these analyses was restricted to the cervical, thoracic, and lumbar spine, rib cage, and sternum. The regions highlighted in red represent hypermineralized tissue within the region of interest. (*B*) The volume of hypermineralized tissue grew exponentially with age in the *ENT1*$^{-/-}$ mice. (*C*) *ENT1*$^{-/-}$ mice also showed increased volume of mineralized tissue with normal bone density (consisting of both bone and ectopic calcifications). Whereas the WT animals appeared to reach a plateau (of approximately 355 mm^3 by day 200), the *ENT1*$^{-/-}$ mice reached a plateau (552 mm^3) by day 400. (*D*) Likewise, the maximum mineral density of the WT mice reached a plateau before an age of 200 days, whereas that of the *ENT1*$^{-/-}$ mice continued to increase past day 400. In *B* through *D*, the symbols represent μCT-derived parameters for individual mice and the lines represent the nonlinear fits.

mineralized tissue density observed using μCT. The calcium/phosphorus ratio was similar in all samples.

Histological appearance of mineralized lesions

We first assessed the intervertebral disc regions of wild-type and *ENT1*$^{-/-}$ mice between 12 and 17 months of age. Decalcified sections stained with H&E revealed the presence in *ENT1*$^{-/-}$ mice of large accumulations of amorphous, eosinophilic acellular material suggestive of niduses of mineralization in the cervical, thoracic, lumbar, and caudal regions (Fig. 4). Interestingly, in the intervertebral disc, lesions appeared to be localized within the annulus fibrosus, leading to lateral compression of the nucleus pulposus and extensive bulging of the annulus fibrosus out of the intervertebral space (Fig. 4, right panels). There was no evidence that lesions were associated with inflammation or

Table 2. Energy-Dispersive X-Ray Spectroscopy

		% Atomic ratio				
Location	Genotype	Carbon	Oxygen	Phosphorous	Calcium	Ca/P Ratio
Vertebra	WT	45.1 ± 4.8	34.0 ± 1.8	7.4 ± 0.7	12.7 ± 2.3	1.7 ± 0.1
	ENT1$^{-/-}$	45.6 ± 2.2	37.5 ± 0.9	6.8 ± 0.5	10.5 ± 0.6	1.6 ± 0.1
Lesion	*ENT1*$^{-/-}$	37.6 ± 3.5	41.6 ± 2.3	8.7 ± 0.4*	13.3 ± 1.1*	1.5 ± 0.1

Scanning electron microscopy was used to identify regions of vertebral cortical bone and ectopic mineralization (lesion) in samples isolated from 6-month-old WT and *ENT1*$^{-/-}$ mice. Energy-dispersive X-ray spectroscopy was then applied to these selected regions to obtain the % atomic ratios of the indicated elements. Data are mean ± SEM, $n = 4$.

WT = wild-type; ENT1 = equilibrative nucleoside transporter 1.

*Significant difference between lesion and *ENT1*$^{-/-}$ vertebra ($p < 0.05$; Student's *t* test).

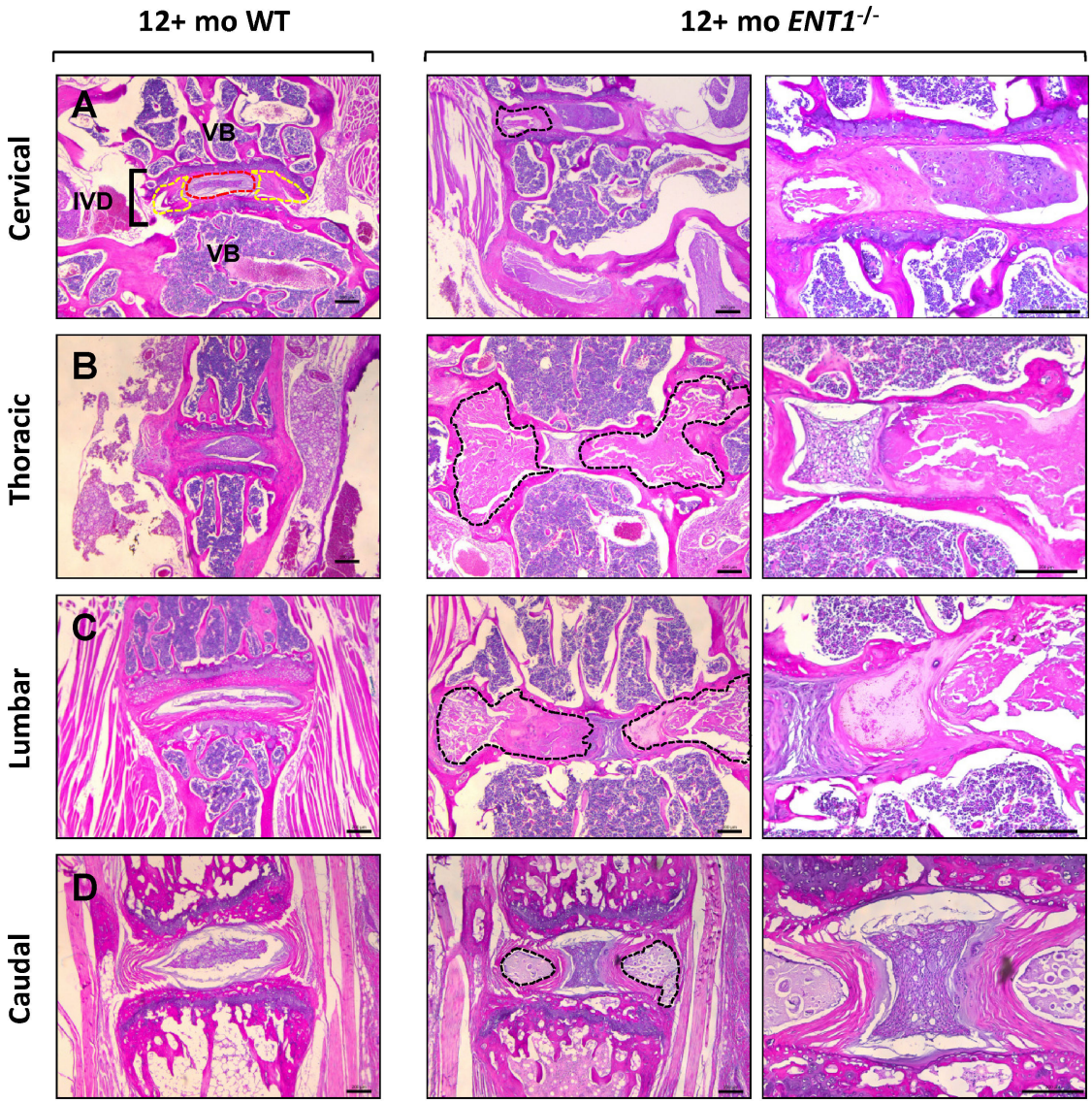

Fig. 4. Histological appearance of spinal tissues in cervical (*A*), thoracic (*B*), lumbar (*C*), and caudal (*D*) spines of 12 + -month-old wild-type (WT) and *ENT1*$^{-/-}$ mice. In *A*, vertebral structures are indicated: the intervertebral disc (IVD) is formed by the annulus fibrosus outlined in yellow and nucleus pulposus outline in red, which are located between adjacent vertebral bones (VB). The spines of *ENT1*$^{-/-}$ mice show irregular lesions within the annulus fibrosus of the IVD. Lesions are encapsulated by layers of fibrocartilaginous cells. Lesions are outlined with black dashed lines and are shown at higher magnification in the panels to the right. Samples were sectioned in the coronal plane and stained with hematoxylin and eosin (H&E). Images are oriented with rostral at the top and are representative of 3 animals of each genotype 12 to 17 months of age. Scale bars represent 200 μm.

increased vascularization. Because the sacral intervertebral discs undergo progressive fusion with the onset of skeletal maturity in mice, this region was not examined for ectopic mineralization.

Lesions were also detected in the sternocostal region of *ENT1*$^{-/-}$ mice between 12 and 17 months of age, by both μCT and histology (Figs. 2, 3*A*, and Supplemental Fig. S4*A*). In this region, extensive ectopic mineral was detected within the connective tissue of the sternocostal articulations, leading to deformation of the sternum. In contrast, examination of appendicular joints revealed no aberrant morphology or evidence of ectopic mineralization (Supplemental Fig. S4*B*–*E*) establishing that lesions are specifically associated with the axial skeleton.

Comparison of histological sections of spinal tissues from wild-type and *ENT1*$^{-/-}$ mice at 6 months of age revealed further insights into the development of lesions. Within the cervical spine of 6-month-old *ENT1*$^{-/-}$ mice, large lesions were associated with the paraspinal ligaments, but no distinct lesions were detected within the intervertebral discs in this region (Fig. 5*A*). However, the outer annulus fibrosus of the intervertebral discs did appear altered, with regions of metaplasia and disruption of normal tissue architecture (Fig. 5*A*, arrowhead). Within the thoracic spine of 6-month-old *ENT1*$^{-/-}$ mice, extensive lesions were localized within: (1) the annulus fibrosus; (2) the fibrocartilaginous tissue of the posterior paraspinal ligaments; and (3) the fibrocartilaginous tissue of the rib entheses (Fig. 5*B*). In the lumbar spine of 6-month-old *ENT1*$^{-/-}$ mice, small lesions were detected within the annulus fibrosus, leading to disruption of intervertebral disc structure and displacement of the nucleus pulposus (Fig. 5*C*). At this time point, no changes were detected within the caudal spine.

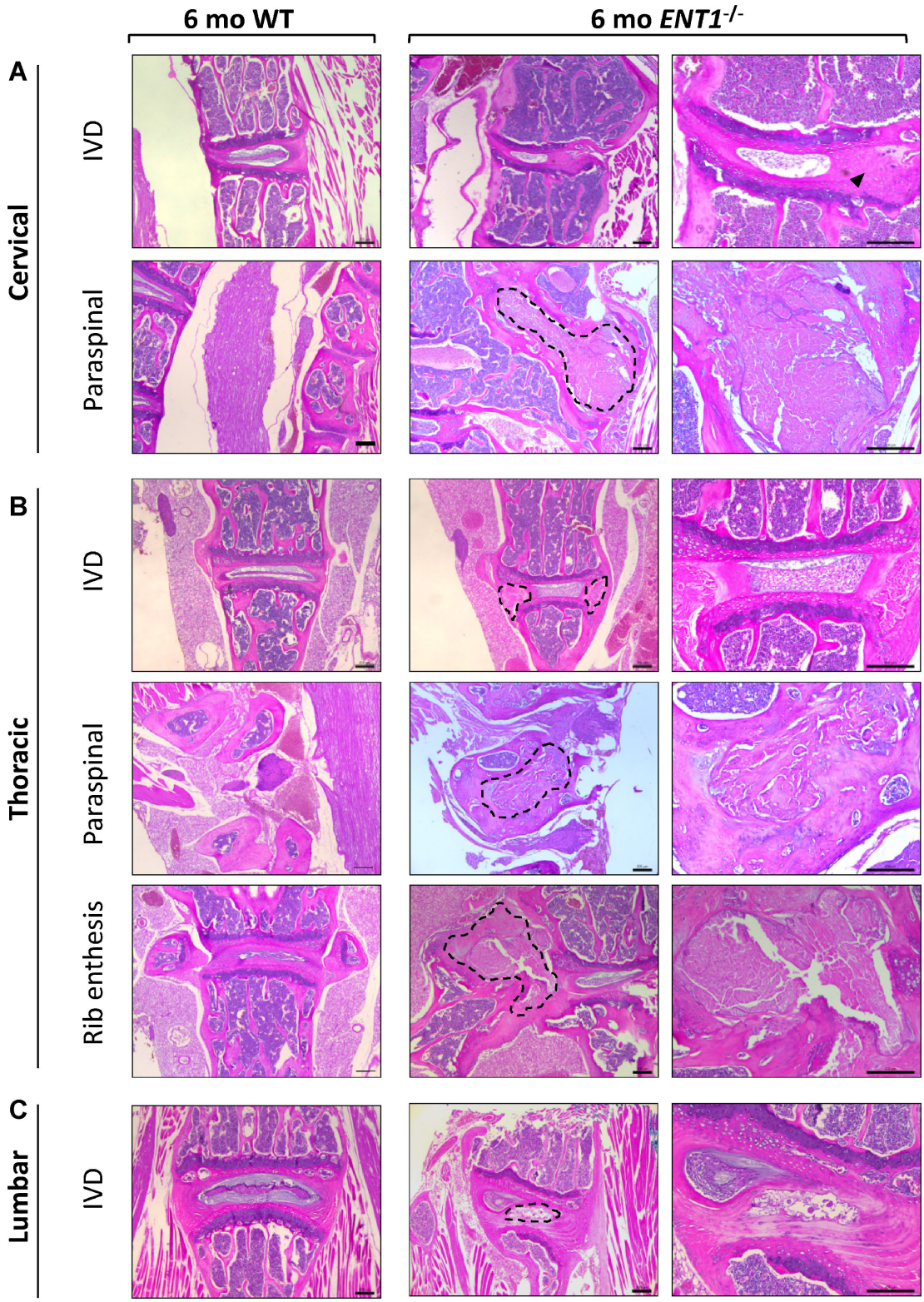

Fig. 5. Histological appearance of spinal tissues in cervical (*A*), thoracic (*B*), and lumbar (*C*) spine segments from 6-month-old wild-type (WT) and *ENT1*$^{-/-}$ mice. Representative images demonstrate the location of lesions consisting of irregular accumulations of eosinophilic material in the intervertebral disc (IVD), paraspinal ligaments, and rib entheses in *ENT1*$^{-/-}$ mice. Lesions are outlined with black dashed lines and tissues are shown at higher magnification in the panels to the right. Arrowhead in *A* indicates a nonmineralized region of metaplasia accompanied by disruption of normal tissue architecture in the annulus fibrosus of the IVD. Images are oriented with rostral at the top and are representative of 3 animals of each genotype. Scale bars represent 200 μm.

At 2 months of age, when ectopic mineral was first detected in *ENT1*$^{-/-}$ mice by μCT, histological examination also demonstrated lesions within the paraspinal ligaments of the cervical spine (Fig. 6*A*). Interestingly, these lesions were associated with large regions of metaplasia, with a disruption of normal tissue architecture and increased cellularity (Fig. 6*A*, arrowheads). In the upper thoracic spine, the mineralized lesions detected by μCT in *ENT1*$^{-/-}$ mice were localized to the fibrocartilaginous structures of the paraspinal ligaments and rib entheses, within larger regions demonstrating evidence of hyperplasia and desmoplasia (Fig. 6*B*, arrowheads). At this time point, no lesions were detectable in intervertebral discs within any region of the spine. Early lesions evident at 2 months of age were surrounded by a clearly demarcated transition zone (TZ; Fig. 6*C*). The periphery of this zone consisted of typical fibrocartilaginous tissue and, as expected, cells with basophilic nuclei that stained positively with DAPI (Fig. 6*C*, lower panels). However, the more central region of the transition zone was characterized by metaplasia, with cells displaying eosinophilic nuclei that stained positively with DAPI, revealing an intact nuclear structure. The TZ surrounded the presumptive mineralized lesion, which contained large accumulations of amorphous matrix and necrotic cell debris. There was no evidence of apoptotic nuclei within the lesion or TZ.

Differences in blood chemistry and gene expression associated with the *ENT1*$^{-/-}$ phenotype

Blood plasma or serum from 2-month-old wild-type and *ENT1*$^{-/-}$ mice was analyzed for components related to mineralization as well as adenosine and adenosine metabolites (Table 3). HPLC analysis of plasma showed 2.8-fold greater adenosine levels in *ENT1*$^{-/-}$ than wild-type mice. In contrast, there were no significant differences in levels of the adenosine metabolites xanthine and uric acid, arguing against the possibility that ectopic lesions involved deposition of monosodium urate crystals. Importantly, serum levels of alkaline phosphatase, calcium, phosphate, and magnesium were not significantly different in *ENT1*$^{-/-}$ and wild-type mice. On the other hand, quantification of plasma PP_i levels revealed 3.4 ± 1.0-fold greater levels in *ENT1*$^{-/-}$ mice than in wild-type controls ($n = 6$ two-month-old mice for each genotype, $p < 0.05$).

Given this alteration in PP_i levels, we interrogated the expression of genes associated with pyrophosphate metabolism in intervertebral disc tissues isolated from *ENT1*$^{-/-}$ and wild-type littermate control mice at 6 months of age. Real-time PCR analysis demonstrated a significant decrease in the expression of ectonucleotide pyrophosphatase/phosphodiesterase 1 (*Enpp1*; Fig. 7*A*), *Ank* (a putative PP_i transporter) (Fig. 7*B*), and tissue-nonspecific alkaline phosphatase (*Alpl*; Fig. 7*C*) in *ENT1*$^{-/-}$ mice. In contrast, no significant difference was detected in the expression of unrelated genes including the adenosine A3 receptor (*Adora3*; Fig. 7*D*) in *ENT1*$^{-/-}$ and wild-type mice, indicating specificity.

To determine if the specific anatomical pattern of ectopic mineralization was influenced by endogenous levels of *ENT1*, expression was assessed in 6-month-old wild-type mice. No differences were detected in *ENT1* transcript levels in intervertebral disc tissues isolated from cervical-thoracic, lumbar, or caudal regions of the spinal column (Fig. 7*E*).

Discussion

This is the first report of a role for ENT1 in regulating biomineralization. We discovered that *ENT1*$^{-/-}$ mice develop ectopic mineralization with distribution restricted to the fibrous connective tissues of the spine and sternum. In the spine, pathological mineralization begins in the paraspinal fibrocartilaginous tissues and progresses to involve the annulus fibrosus of intervertebral discs. Aberrant mineralization is first observed in *ENT1*$^{-/-}$ mice between 6 and 8 weeks of age in the paraspinal connective tissues of the cervical vertebrae. With advancing age, lesions increase in severity and progress to other regions of the spine, with ectopic mineralization eventually involving the thoracic, lumbar, and caudal spine, as well as the sternocostal articulations.

ENT1$^{-/-}$ mice were first used to investigate the role of adenosine transport in the central nervous system pathways regulating alcohol consumption.[32] In that study, male mice were examined at approximately 10 weeks of age and appeared normal in their anatomy, physiology, mortality rates, and consumption of water. However, *ENT1*$^{-/-}$ mice consumed twice as much alcohol compared to wild-type controls. This behavior was associated with a decrease in endogenous adenosine tone, which was not due to loss of A_1 receptors or decreases in A_1 receptor affinity. *ENT1*$^{-/-}$ mice have also been shown to exhibit reduced anxiety-like behaviors.[43] Levels of endogenous extracellular adenosine were not reported in these studies.

More recently, *ENT1*-null mice have been used to investigate the role of this transporter in the cardiovascular system. Microvascular endothelial cells isolated from *ENT1*$^{-/-}$ mice have enhanced expression of the A_{2A} adenosine receptor and adenosine deaminase.[33] Cardiomyocytes and microvascular endothelial cells from *ENT1*$^{-/-}$ mice are relatively resistant to ischemic insult and *ENT1*$^{-/-}$ mice show decreased heart damage in response to ischemia and hypoxia.[44] Furthermore, loss of ENT1 protects against ischemic acute kidney injury through control of postischemic renal perfusion.[45] Overall, these studies point to a cardioprotective role of ENT1. However, it is unlikely that changes in the nervous and cardiovascular systems give rise to ectopic mineralization in *ENT1*$^{-/-}$ mice, especially of the inner annulus fibrosus, which is considered an avascular and aneural tissue.[46,47]

In the present study, we found that plasma adenosine concentrations are significantly elevated in the *ENT1*$^{-/-}$ mice compared to wild-type littermates, as reported previously.[41] The greater plasma concentration of adenosine in *ENT1*$^{-/-}$ mice likely reflects extracellular accumulation of adenosine due to lack of uptake by cells that normally express ENT1, one of the primary uptake pathways for adenosine.[31,48] The role of elevated extracellular adenosine in the formation of abnormal mineral deposits in fibrocartilaginous tissues remains to be explored, but may involve local changes in adenosine receptor signaling.

In this regard, recent advances point to a critical role for purine metabolism and signaling in the regulation of biomineralization and in diseases associated with either insufficient or ectopic mineralization.[25–30] Once released by the cell, extracellular adenosine triphosphate (ATP) is sequentially metabolized by

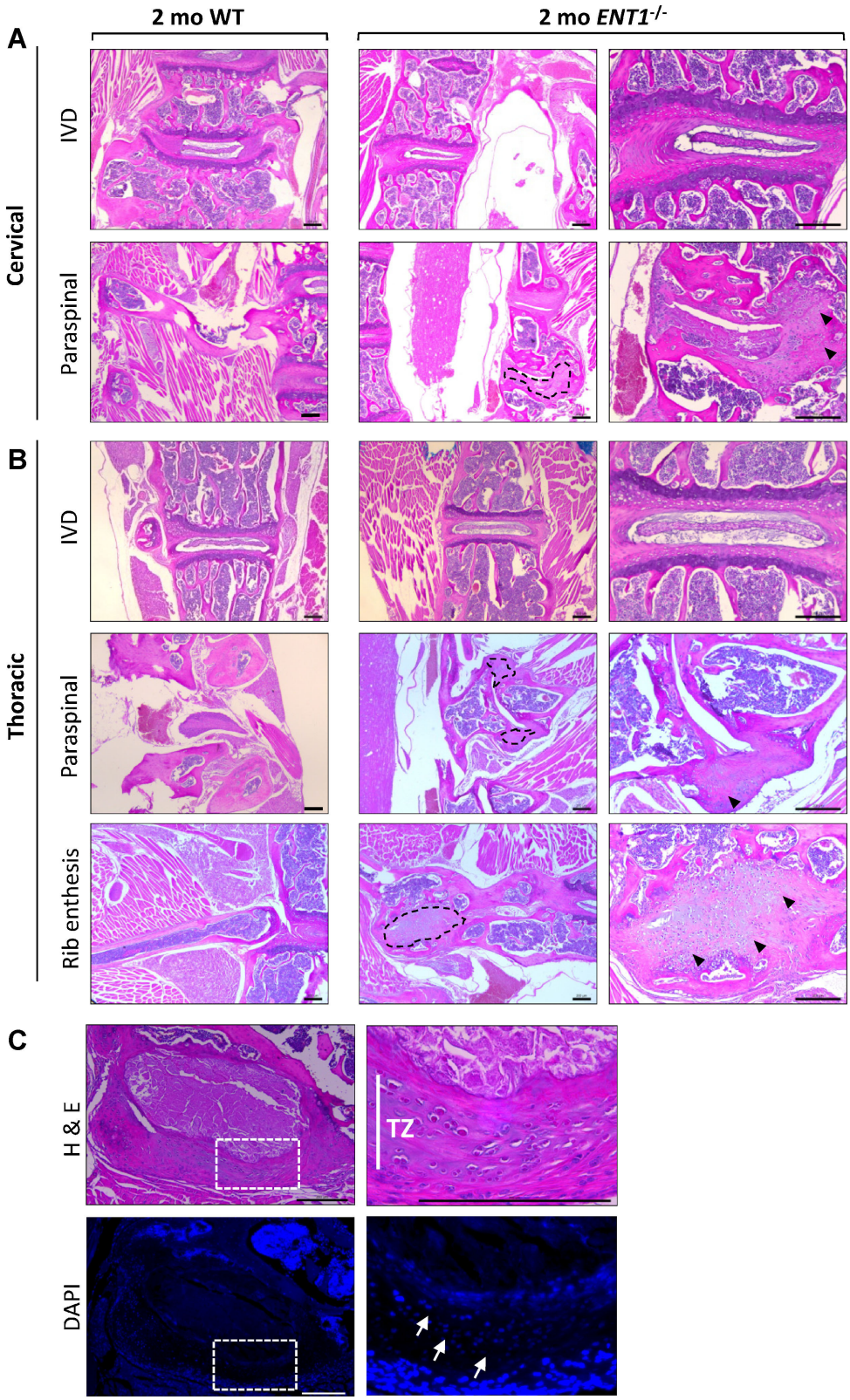

Fig. 6. Histological appearance of the intervertebral disc (IVD), paraspinal ligaments, and rib entheses in cervical (*A*) and thoracic (*B*) spine segments from 2-month-old wild-type (WT) and *ENT1*$^{-/-}$ mice. Lesions are outlined with black dashed lines and tissues are shown at higher magnification in the panels to the right. Arrowheads indicate regions demonstrating tissue metaplasia. (*C*) Serial sections of representative lesion localized to the paraspinal tissue of the thoracic spine of a 2-month-old *ENT1*$^{-/-}$ mouse stained with H&E (top panel) and DAPI (bottom panel). Cells with eosinophilic nuclei are detected in the transition zone (TZ) between normal fibrocartilaginous tissues and lesion. DAPI staining demonstrates that these cells retain an intact nuclear structure (arrows indicate individual cells). Images are oriented with rostral at the top and are representative of at least 3 animals of each genotype. Scale bars represent 200 μm.

Table 3. Blood Chemistry

	Wild-type ($n = 4$)	*ENT1*$^{-/-}$ ($n = 5$)
Adenosine (μM)	2.2 ± 0.4	$6.2 \pm 1.4^{*}$
Xanthine (μM)	4.3 ± 1.5	5.2 ± 2.4
Uric acid (μM)	163 ± 23	176 ± 14
ALP (IU/L)	97 ± 9	109 ± 10
Ca (mM)	2.30 ± 0.03	2.31 ± 0.02
Mg (mM)	1.26 ± 0.04	1.30 ± 0.08
P_i (mM)	3.1 ± 0.3	3.7 ± 0.4

Data are means ± SEM. Serum or plasma was obtained from wild-type and *ENT1*$^{-/-}$ mice at 2 months of age.

ALP = total alkaline phosphatase; ENT1 = equilibrative nucleoside transporter 1; P_i = inorganic phosphate.

*Significantly different from wild-type ($p < 0.05$, Student's *t* test).

cell-surface enzymes, leading first to the production of PP_i and adenosine monophosphate (AMP), which in turn are converted to inorganic phosphate and adenosine. Ectonucleotide pyrophosphatase/phosphodiesterase 1 (Enpp1) is responsible for the first step in this process, and the release of PP_i has been shown to inhibit ectopic calcification in soft tissues.[49] Interestingly, we show that *ENT1*-null mice demonstrate significant downregulation of *Enpp1* expression in intervertebral disc tissues relative to wild-type littermate controls. These findings are in keeping with the reported association between mutations in the gene encoding Enpp1 and hypermineralization disorders such as idiopathic infantile calcification[25] and OPLL.[26] Furthermore, *Enpp1*$^{-/-}$ mice display soft tissue mineralization in the Achilles tendon, paraspinal ligaments, and intervertebral discs, as well as hyperostosis of peripheral joints and calcification of articular

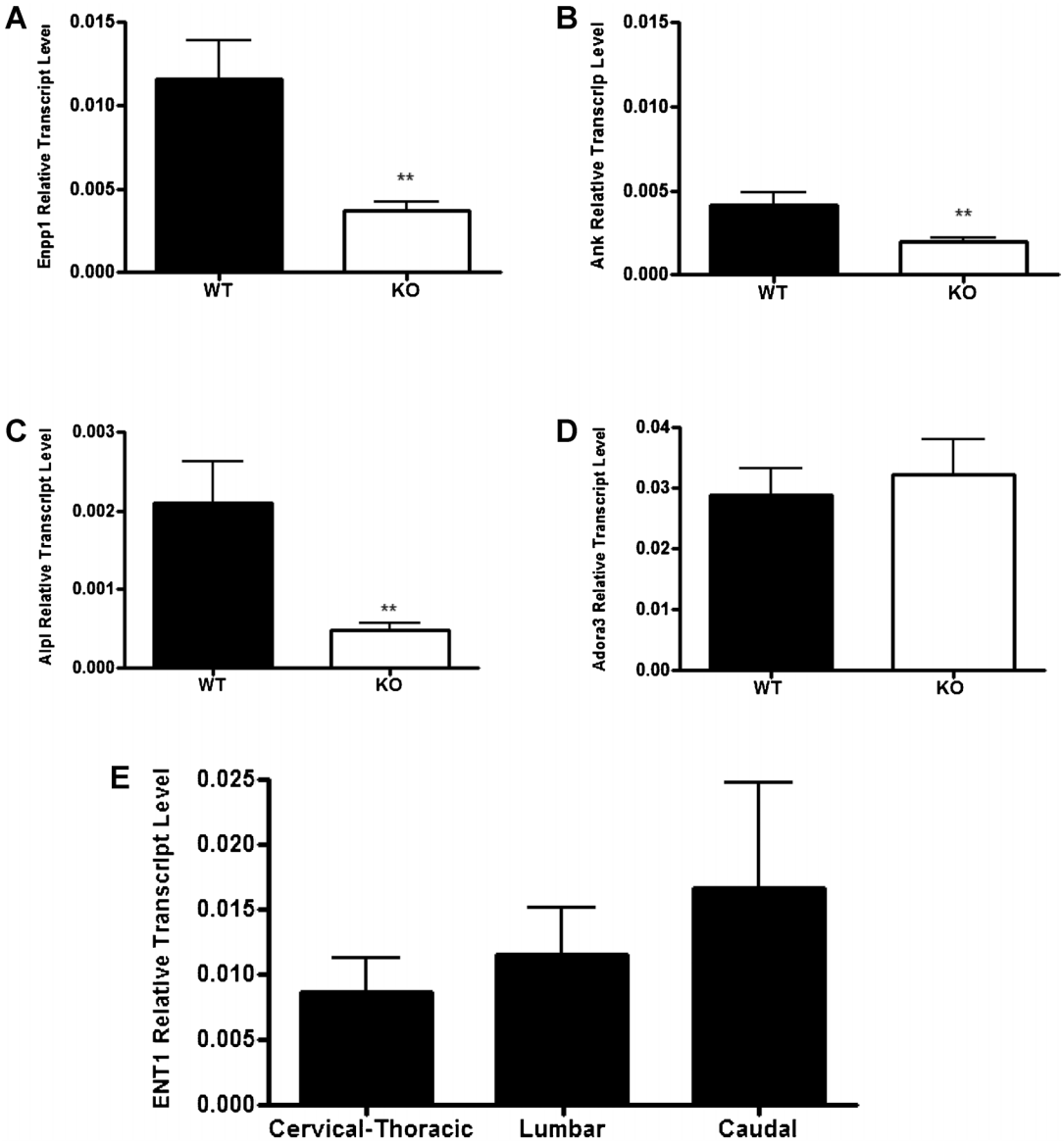

Fig. 7. Gene expression analysis of intervertebral disc tissues isolated from 6-month-old wild-type (WT) and *ENT1*$^{-/-}$ (KO) mice. Real-time PCR analysis of genes associated with PP_i metabolism and tissue mineralization revealed significant reductions in the expression of (*A*) Enpp1, (*B*) Ank, and (*C*) Alpl in *ENT1*$^{-/-}$ mice compared to wild-type controls. (*D*) In contrast, there was no significant difference in the expression of the adenosine A_3 receptor (Adora3), indicating specificity of changes in gene expression. (*E*) Real-time PCR analysis of ENT1 expression revealed no significant differences between anatomical regions of the spine in wild-type mice. Data are means ± SEM; $n = 8$ animals each genotype. **Significantly different from wild-type ($p < 0.01$, Student's *t* test).

cartilage.[50] However, elements of the appendicular skeleton are not affected in *ENT1*$^{-/-}$ mice; changes are limited to fibrocartilaginous tissues of the axial skeleton.

We also observed a significant decrease in *Ank* expression in the intervertebral discs of *ENT1*$^{-/-}$ mice. Ank is a transmembrane protein that is thought to mediate PP_i transport. In mice, loss-of-function mutations of *Ank* lead to arthritis, ectopic crystal formation, and generalized joint fusion,[51] whereas, in humans, dominant mutations are associated with craniometaphyseal dysplasia[52,53] and familial chondrocalcinosis.[54,55] Thus, like *Enpp1*, decreased *Ank* expression in the spinal tissues of *ENT1*$^{-/-}$ mice would be expected to further suppress extracellular PP_i levels, permitting the formation of ectopic mineral deposits.

Unexpectedly, expression of *Alpl* was also found to be decreased in the intervertebral discs of ENT1-null mice. *Alpl* encodes tissue-nonspecific alkaline phosphatase, which is responsible for the hydrolysis PP_i,[50] and *Alpl* expression has been shown previously to be regulated by extracellular adenosine.[27] In humans, disruption of *ALPL* causes hypophosphatasia, characterized by skeletal hypomineralization[56] and presumably a result of excessive accumulation of PP_i. Thus, decreased *Alpl* expression in the spinal tissues of *ENT1*$^{-/-}$ mice would be expected to increase extracellular PP_i levels, counteracting the decrease in PP_i arising from changes in *Enpp1* and *Ank* expression. Moreover, it is conceivable that a generalized decrease in *Alpl* expression could account for the increase in plasma PP_i that we observed in *ENT1*$^{-/-}$ mice.

Adenosine and ATP can regulate cell behavior and gene expression through cell surface receptors—the adenosine receptor family[57] and the P2 family of nucleotide receptors,[58,59] respectively. Adenosine increases intracellular cyclic AMP (cAMP) levels via its A_{2A} and A_{2B} receptor subtypes. cAMP has been shown to induce abnormal calcification of vascular smooth muscle cells via a mechanism involving reduction in extracellular PP_i accumulation.[60,61] In addition, activation of the P2X7 subtype of ATP receptors promotes bone formation and mineralization.[59,62]

Taken together, our data suggest that disruption of adenosine signaling and PP_i metabolism in *ENT1*$^{-/-}$ mice is associated with disease onset and progression. Although there are no reported associations between mutations in the gene encoding ENT1 in humans and DISH, the high incidence of this disease in the human population argues against an underlying single gene defect. However, disruption of adenosine or PP_i metabolism could result from alterations in the function of one or more regulatory or metabolic proteins—either through genetic defects or as a consequence of cell aging.

In *ENT1*$^{-/-}$ mice, the only location outside of the spine that exhibited ectopic mineralization was the sternocostal region. This distinct anatomical pattern of mineral deposition in *ENT1*$^{-/-}$ mice suggests that some common element in spinal and sternal fibrocartilaginous tissues makes them susceptible to ectopic mineralization in the absence of ENT1. Relatively scant vascular perfusion of the affected fibrocartilaginous tissues could lessen the clearance of extracellular adenosine, giving rise to sustained adenosine signaling, which may in turn lead to deregulation of PP_i metabolism.

The spatial and temporal pattern of ectopic mineralization observed in the *ENT1*$^{-/-}$ mice, along with the absence of inflammation in affected tissues, resemble characteristics of DISH in humans. DISH affects about 20% of the male population over the age of 55 years, with a slightly lower prevalence in women.[34] Similarly, in *ENT1*$^{-/-}$ mice, lesions developed gradually over time, with functional impairments noticeable by 8 months of age. Similar to DISH in humans, which is often first diagnosed in the cervical or thoracic spine,[63] lesions in *ENT1*$^{-/-}$ mice began in the cervicothoracic spine and spread caudally. Moreover, sternal involvement is also noted in DISH patients.[64] On the other hand, extra-axial calcifications are present in some DISH patients, but were not detected by μCT or histology in *ENT1*$^{-/-}$ mice. Interestingly, the reproducible pattern of mineral deposition observed in *ENT1*$^{-/-}$ mice was not related to differences in endogenous *ENT1* expression levels in the affected tissues. The factors contributing to the timing of mineral deposition at these sites remains an intriguing question for ongoing investigation. The radiographic appearance of DISH in humans bears striking resemblance to that of ectopic mineralization in *ENT1*$^{-/-}$ mice. DISH is characterized by tortuous paravertebral calcifications generally anterior to the vertebral bodies.[65] On gross examination the appearance is likened to that of candle wax dripping down the spine. This appearance is remarkably similar to that observed in the present study by μCT analysis of *ENT1*$^{-/-}$ mice.

In summary, this is the first report of a role for the primary membrane transporter for adenosine, ENT1, in regulating the calcification of soft tissues. Disruption of purine homeostasis by removal of ENT1 leads to the ectopic mineralization of paraspinal ligaments and intervertebral discs in mice, resembling lesions seen in the human condition, DISH. Pathogenesis appears to be associated with both local and systemic changes in PP_i homeostasis. The *ENT1*$^{-/-}$ mouse may prove useful as a model for investigating the mechanisms underlying ectopic mineralization associated with DISH and for the evaluation of therapies for the prevention and reversal of DISH and associated pathologies.

Disclosures

All authors state that they have no conflicts of interest.

Acknowledgments

These studies were funded by the Canadian Institutes of Health Research (CIHR) (MOP-115068) and the Canadian Arthritis Network (CAN) (10-DAP-11). DBJB was supported by a CIHR Doctoral Research Award. DWH holds the Dr. Sandy Kirkley Chair in Musculoskeletal Research at The University of Western Ontario. CAS is supported by a Network Scholar Award from The Arthritis Society and CAN. MD is a Career Investigator of the Heart and Stroke Foundation of Ontario. We thank: Tom Chrones, Holly Dupuis, and Linda Jackson for assistance with histology; Joseph Umoh for μCT scanning; Drs. Tom Daley and Ian Welch for guidance on histopathology; Drs. David Freeman and Murray Cutler for help with HPLC analyses; and Dr. Todd Simpson

(Western Nanofabrication Laboratory) for assistance with SEM and EDX. Requests for *ENT1*$^{-/-}$ mice should be addressed to Dr. Doo-Sup Choi, Department of Molecular Pharmacology and Experimental Therapeutics, Mayo Clinic College of Medicine, Rochester, MN 55905, USA.

Authors' roles: Study design: SJD, JRH, and CAS. Data collection: SW, DBJB, DQ, HI, and DWH. Data analysis: SW, DBBJ, HI, DWH, MD, JRH, and CAS. Data interpretation: SW, DBJB, DSC, DWH, MD, SJD, JRH, and CAS. Drafting manuscript: SW, DBJB, DWH, and MD. Revising manuscript content: DSC, SJD, JRH, MD, and CAS. Approving final version of manuscript: all authors. JRH and CAS take responsibility for the integrity of the data analysis.

References

1. Toussaint ND. Extracellular matrix calcification in chronic kidney disease. Curr Opin Nephrol Hypertens. 2011;20(4):360–8.
2. Demer LL, Tintut Y. Vascular calcification: pathobiology of a multifaceted disease. Circulation. 2008;117(22):2938–48.
3. Persy V, D'Haese P. Vascular calcification and bone disease: the calcification paradox. Trends Mol Med. 2009;15(9):405–16.
4. Mader R, Buskila D, Verlaan JJ, Atzeni F, Olivieri I, Pappone N, Di Girolamo C, Sarzi-Puttini P. Developing new classification criteria for diffuse idiopathic skeletal hyperostosis: back to square one. Rheumatology (Oxford). 2012.
5. Saetia K, Cho D, Lee S, Kim DH, Kim SD. Ossification of the posterior longitudinal ligament: a review. Neurosurg Focus. 2011;30(3):E1.
6. Olivieri I, D'Angelo S, Palazzi C, Padula A, Mader R, Khan MA. Diffuse idiopathic skeletal hyperostosis: differentiation from ankylosing spondylitis. Curr Rheumatol Rep. 2009;11(5):321–8.
7. Resnick D, Niwayama G. Radiographic and pathologic features of spinal involvement in diffuse idiopathic skeletal hyperostosis (DISH). Radiology. 1976;119(3):559–68.
8. Johnsson KE, Petersson H, Wollheim FA, Saveland H. Diffuse idiopathic skeletal hyperostosis (DISH) causing spinal stenosis and sudden paraplegia. J Rheumatol. 1983;10(5):784–9.
9. Wilson FM, Jaspan T. Thoracic spinal cord compression caused by diffuse idiopathic skeletal hyperostosis (DISH). Clin Radiol. 1990; 42(2):133–5.
10. Seidler TO, Perez Alvarez JC, Wonneberger K, Hacki T. Dysphagia caused by ventral osteophytes of the cervical spine: clinical and radiographic findings. Eur Arch Otorhinolaryngol. 2009;266(2): 285–91.
11. Diederichs G, Engelken F, Marshall LM, Peters K, Black DM, Issever AS, Barrett-Connor E, Orwoll E, Hamm B, Link TM. Diffuse idiopathic skeletal hyperostosis (DISH): relation to vertebral fractures and bone density. Osteoporos Int. 2011;22(6):1789–97.
12. Verdone F. Diffuse idiopathic skeletal hyperostosis in the third millennium: is there (yet) cause for concern? J Rheumatol. 2010; 37(6):1356–7.
13. Kiss C, Szilagyi M, Paksy A, Poor G. Risk factors for diffuse idiopathic skeletal hyperostosis: a case-control study. Rheumatology (Oxford). 2002;41(1):27–30.
14. Mader R, Lavi I. Diabetes mellitus and hypertension as risk factors for early diffuse idiopathic skeletal hyperostosis (DISH). Osteoarthritis Cartilage. 2009;17(6):825–8.
15. Mader R, Novofestovski I, Adawi M, Lavi I. Metabolic syndrome and cardiovascular risk in patients with diffuse idiopathic skeletal hyperostosis. Semin Arthritis Rheum. 2009;38(5):361–5.
16. Mader R. Diffuse idiopathic skeletal hyperostosis: time for a change. J Rheumatol. 2008;35(3):377–9.
17. Tsukahara S, Miyazawa N, Akagawa H, Forejtova S, Pavelka K, Tanaka T, Toh S, Tajima A, Akiyama I, Inoue I. COL6A1, the candidate gene for ossification of the posterior longitudinal ligament, is associated with diffuse idiopathic skeletal hyperostosis in Japanese. Spine (Phila Pa 1976). 2005;30(20):2321–4.
18. Jun JK, Kim SM. Association study of fibroblast growth factor 2 and fibroblast growth factor receptors gene polymorphism in Korean ossification of the posterior longitudinal ligament patients. J Korean Neurosurg Soc. 2012;52(1):7–13.
19. Okawa A, Ikegawa S, Nakamura I, Goto S, Moriya H, Nakamura Y. Mapping of a gene responsible for twy (tip-toe walking Yoshimura), a mouse model of ossification of the posterior longitudinal ligament of the spine (OPLL). Mamm Genome. 1998;9(2):155–6.
20. Okawa A, Nakamura I, Goto S, Moriya H, Nakamura Y, Ikegawa S. Mutation in Npps in a mouse model of ossification of the posterior longitudinal ligament of the spine. Nat Genet. 1998;19(3):271–3.
21. Sakou T, Taketomi E, Matsunaga S, Yamaguchi M, Sonoda S, Yashiki S. Genetic study of ossification of the posterior longitudinal ligament in the cervical spine with human leukocyte antigen haplotype. Spine (Phila Pa 1976). 1991;16(11):1249–52.
22. Tanaka T, Ikari K, Furushima K, Okada A, Tanaka H, Furukawa K, Yoshida K, Ikeda T, Ikegawa S, Hunt SC, Takeda J, Toh S, Harata S, Nakajima T, Inoue I. Genomewide linkage and linkage disequilibrium analyses identify COL6A1, on chromosome 21, as the locus for ossification of the posterior longitudinal ligament of the spine. Am J Hum Genet. 2003;73(4):812–22.
23. Wozney JM, Rosen V, Celeste AJ, Mitsock LM, Whitters MJ, Kriz RW, Hewick RM, Wang EA. Novel regulators of bone formation: molecular clones and activities. Science. 1988;242(4885):1528–34.
24. Kamiya M, Harada A, Mizuno M, Iwata H, Yamada Y. Association between a polymorphism of the transforming growth factor-beta1 gene and genetic susceptibility to ossification of the posterior longitudinal ligament in Japanese patients. Spine (Phila Pa 1976). 2001;26(11):1264-6.
25. Rutsch F, Ruf N, Vaingankar S, Toliat MR, Suk A, Hohne W, Schauer G, Lehmann M, Roscioli T, Schnabel D, Epplen JT, Knisely A, Superti-Furga A, McGill J, Filippone M, Sinaiko AR, Vallance H, Hinrichs B, Smith W, Ferre M, Terkeltaub R, Nurnberg P. Mutations in ENPP1 are associated with 'idiopathic' infantile arterial calcification. Nat Genet. 2003;34(4):379–81.
26. Armas JB, Couto AR, Bettencourt BF. Spondyloarthritis, diffuse idiopathic skeletal hyperostosis (DISH) and chondrocalcinosis. Adv Exp Med Biol. 2009;649:37–56.
27. St Hilaire C, Ziegler SG, Markello TC, Brusco A, Groden C, Gill F, Carlson-Donohoe H, Lederman RJ, Chen MY, Yang D, Siegenthaler MP, Arduino C, Mancini C, Freudenthal B, Stanescu HC, Zdebik AA, Chaganti RK, Nussbaum RL, Kleta R, Gahl WA, Boehm M. NT5E mutations and arterial calcifications. N Engl J Med. 2011;364(5): 432–42.
28. Yadav MC, Simao AM, Narisawa S, Huesa C, McKee MD, Farquharson C, Millan JL. Loss of skeletal mineralization by the simultaneous ablation of PHOSPHO1 and alkaline phosphatase function: a unified model of the mechanisms of initiation of skeletal calcification. J Bone Miner Res. 2011;26(2):286–97.
29. Mebarek S, Hamade E, Thouverey C, Bandorowicz-Pikula J, Pikula S, Magne D, Buchet R. Ankylosing spondylitis, late osteoarthritis, vascular calcification, chondrocalcinosis and pseudo gout: toward a possible drug therapy. Curr Med Chem. 2011;18(14):2196–203.
30. Evans BA. Does adenosine play a role in bone formation, resorption and repair? Purinergic Signal. 2012;8(2):177–80.
31. Baldwin SA, Beal PR, Yao SY, King AE, Cass CE, Young JD. The equilibrative nucleoside transporter family. SLC29. Pflugers Arch. 2004;447(5):735–43.
32. Choi DS, Cascini MG, Mailliard W, Young H, Paredes P, McMahon T, Diamond I, Bonci A, Messing RO. The type 1 equilibrative nucleoside

transporter regulates ethanol intoxication and preference. Nat Neurosci. 2004;7(8):855–61.

33. Bone DB, Choi DS, Coe IR, Hammond JR. Nucleoside/nucleobase transport and metabolism by microvascular endothelial cells isolated from ENT1$^{-/-}$ mice. Am J Physiol Heart Circ Physiol. 2010;299(3): H847–56.
34. Weinfeld RM, Olson PN, Maki DD, Griffiths HJ. The prevalence of diffuse idiopathic skeletal hyperostosis (DISH) in two large American Midwest metropolitan hospital populations. Skeletal Radiol. 1997; 26(4):222–5.
35. Ulici V, Hoenselaar KD, Agoston H, McErlain DD, Umoh J, Chakrabarti S, Holdsworth DW, Beier F. The role of Akt1 in terminal stages of endochondral bone formation: angiogenesis and ossification. Bone. 2009;45(6):1133–45.
36. Feldkamp LA, Davis LC, Kress JW. Practical cone-beam algorithm. J Opt Soc Am A. 1984;1(6):612–9.
37. Miller LM, Little W, Schirmer A, Sheik F, Busa B, Judex S. Accretion of bone quantity and quality in the developing mouse skeleton. J Bone Miner Res. 2007;22(7):1037–45.
38. Costa DO, Allo BA, Klassen R, Hutter JL, Dixon SJ, Rizkalla AS. Control of surface topography in biomimetic calcium phosphate coatings. Langmuir. 2012;28(8):3871–80.
39. Ramakers BP, Pickkers P, Deussen A, Rongen GA, van den Broek P, van der Hoeven JG, Smits P, Riksen NP. Measurement of the endogenous adenosine concentration in humans in vivo: methodological considerations. Curr Drug Metab. 2008;9(8):679–85.
40. Xu L, Farthing AK, Shi YJ, Meinke PT, Liu K. Conversion of nocathiacin I to nocathiacin acid by a mild and selective cleavage of dehydroalanine. J Org Chem. 2007;72(19):7447–50.
41. Rose JB, Naydenova Z, Bang A, Ramadan A, Klawitter J, Schram K, Sweeney G, Grenz A, Eltzschig H, Hammond J, Choi DS, Coe IR. Absence of equilibrative nucleoside transporter 1 in ENT1 knockout mice leads to altered nucleoside levels following hypoxic challenge. Life Sci. 2011;89(17–18):621–30.
42. Guillen-Gomez E, Pinilla-Macua I, Perez-Torras S, Choi DS, Arce Y, Ballarin JA, Pastor-Anglada M, Diaz-Encarnacion MM. New role of the human equilibrative nucleoside transporter 1 (hENT1) in epithelial-to-mesenchymal transition in renal tubular cells. J Cell Physiol. 2012;227(4):1521–8.
43. Chen J, Rinaldo L, Lim SJ, Young H, Messing RO, Choi DS. The type 1 equilibrative nucleoside transporter regulates anxiety-like behavior in mice. Genes Brain Behav. 2007;6(8):776–83.
44. Rose JB, Naydenova Z, Bang A, Eguchi M, Sweeney G, Choi DS, Hammond JR, Coe IR. Equilibrative nucleoside transporter 1 plays an essential role in cardioprotection. Am J Physiol Heart Circ Physiol. 2010;298(3):H771–7.
45. Grenz A, Bauerle JD, Dalton JH, Ridyard D, Badulak A, Tak E, McNamee EN, Clambey E, Moldovan R, Reyes G, Klawitter J, Ambler K, Magee K, Christians U, Brodsky KS, Ravid K, Choi DS, Wen J, Lukashev D, Blackburn MR, Osswald H, Coe IR, Nurnberg B, Haase VH, Xia Y, Sitkovsky M, Eltzschig HK. Equilibrative nucleoside transporter 1 (ENT1) regulates postischemic blood flow during acute kidney injury in mice. J Clin Invest. 2012;122(2):693–710.
46. Urban JP, Smith S, Fairbank JC. Nutrition of the intervertebral disc. Spine (Phila Pa 1976). 2004;29(23):2700–9.
47. Freemont TJ, LeMaitre C, Watkins A, Hoyland JA. Degeneration of intervertebral discs: current understanding of cellular and molecular events, and implications for novel therapies. Expert Rev Mol Med. 2001;2001:1–10.
48. Jarvis SM, Hammond JR, Paterson AR, Clanachan AS. Species differences in nucleoside transport. A study of uridine transport nitrobenzylthioinosine binding by mammalian erythrocytes. Biochem J. 1982;208(1):83–8.
49. Terkeltaub R. Physiologic and pathologic functions of the NPP nucleotide pyrophosphatase/phosphodiesterase family focusing on NPP1 in calcification. Purinergic Signal. 2006;2(2):371–7.
50. Harmey D, Hessle L, Narisawa S, Johnson KA, Terkeltaub R, Millan JL. Concerted regulation of inorganic pyrophosphate and osteopontin by akp2, enpp1, and ank: an integrated model of the pathogenesis of mineralization disorders. Am J Pathol. 2004;164(4):1199–209.
51. Ho AM, Johnson MD, Kingsley DM. Role of the mouse ank gene in control of tissue calcification and arthritis. Science. 2000;289(5477): 265–70.
52. Nurnberg P, Thiele H, Chandler D, Hohne W, Cunningham ML, Ritter H, Leschik G, Uhlmann K, Mischung C, Harrop K, Goldblatt J, Borochowitz ZU, Kotzot D, Westermann F, Mundlos S, Braun HS, Laing N, Tinschert S. Heterozygous mutations in ANKH, the human ortholog of the mouse progressive ankylosis gene, result in craniometaphyseal dysplasia. Nat Genet. 2001;28(1):37–41.
53. Reichenberger E, Tiziani V, Watanabe S, Park L, Ueki Y, Santanna C, Baur ST, Shiang R, Grange DK, Beighton P, Gardner J, Hamersma H, Sellars S, Ramesar R, Lidral AC, Sommer A, Raposo do, Amaral CM, Gorlin RJ, Mulliken JB, Olsen BR. Autosomal dominant craniometaphyseal dysplasia is caused by mutations in the transmembrane protein ANK. Am J Hum Genet. 2001;68(6):1321–6.
54. Pendleton A, Johnson MD, Hughes A, Gurley KA, Ho AM, Doherty M, Dixey J, Gillet P, Loeuille D, McGrath R, Reginato A, Shiang R, Wright G, Netter P, Williams C, Kingsley DM. Mutations in ANKH cause chondrocalcinosis. Am J Hum Genet. 2002;71(4):933–40.
55. Williams CJ, Zhang Y, Timms A, Bonavita G, Caeiro F, Broxholme J, Cuthbertson J, Jones Y, Marchegiani R, Reginato A, Russell RG, Wordsworth BP, Carr AJ, Brown MA. Autosomal dominant familial calcium pyrophosphate dihydrate deposition disease is caused by mutation in the transmembrane protein ANKH. Am J Hum Genet. 2002;71(4):985–91.
56. Barvencik F, Beil FT, Gebauer M, Busse B, Koehne T, Seitz S, Zustin J, Pogoda P, Schinke T, Amling M. Skeletal mineralization defects in adult hypophosphatasia—a clinical and histological analysis. Osteoporos Int. 2011;22(10):2667–75.
57. Fredholm BB, AP IJ, Jacobson KA, Linden J, Muller CE. International Union of Basic and Clinical Pharmacology. LXXXI. Nomenclature and classification of adenosine receptors—an update. Pharmacol Rev. 2011;63(1):1–34.
58. Armstrong S, Korcok J, Sims SM, Dixon SJ. Activation of transcription factors by extracellular nucleotides in immune and related cell types. Purinergic Signal. 2007;3(1–2):59–69.
59. Grol MW, Panupinthu N, Korcok J, Sims SM, Dixon SJ. Expression, signaling, and function of P2X7 receptors in bone. Purinergic Signal. 2009;5(2):205–21.
60. Gharibi B, Abraham AA, Ham J, Evans BA. Adenosine receptor subtype expression and activation influence the differentiation of mesenchymal stem cells to osteoblasts and adipocytes. J Bone Miner Res. 2011;26(9):2112–24.
61. Prosdocimo DA, Wyler SC, Romani AM, O'Neill WC, Dubyak GR. Regulation of vascular smooth muscle cell calcification by extracellular pyrophosphate homeostasis: synergistic modulation by cyclic AMP and hyperphosphatemia. Am J Physiol Cell Physiol. 2010; 298(3):C702–13.
62. Panupinthu N, Rogers JT, Zhao L, Solano-Flores LP, Possmayer F, Sims SM, Dixon SJ. P2X7 receptors on osteoblasts couple to production of lysophosphatidic acid: a signaling axis promoting osteogenesis. J Cell Biol. 2008;181(5):859–71.
63. Resnick D, Guerra J Jr, Robinson CA, Vint VC. Association of diffuse idiopathic skeletal hyperostosis (DISH) and calcification and ossification of the posterior longitudinal ligament. AJR Am J Roentgenol. 1978;131(6):1049–53.
64. Parker VS, Malhotra CM, Ho G Jr, Kaplan SR. Radiographic appearance of the sternomanubrial joint in arthritis and related conditions. Radiology. 1984;153(2):343–7.
65. Verlaan JJ, Westerveld LA, van Keulen JW, Bleys RL, Dhert WJ, van Herwaarden JA, Moll FL, Oner FC. Quantitative analysis of the anterolateral ossification mass in diffuse idiopathic skeletal hyperostosis of the thoracic spine. Eur Spine J. 2011;20(9):1474–9.